Cooperative Binding of Cytosolic Type III Secretion System Proteins to the Injectisome Revealed by Live-Cell Single-Molecule Localization Microscopy

Olivia I.C. de Cuba[1], Gopika A. Lekshmi[2], Caroline F. Tyndall[2], Andreas Gahlmann[1,3,4,#]

[1] Department of Molecular Physiology & Biological Physics, University of Virginia School of Medicine, Charlottesville, Virginia.

[2] Department of Biology, University of Virginia, Charlottesville, Virginia.

[3] Department of Chemistry, University of Virginia, Charlottesville, Virginia.

[4] Department of Biomolecular Engineering, University of Virginia, Charlottesville, Virginia.

[#] Address correspondence to agahlmann@virginia.edu

ABSTRACT

Type III secretion systems (T3SSs) are employed by many Gram-negative bacteria to translocate virulent effector proteins into host cells. Secretion occurs through the T3SS injectisome, a multi-membrane-spanning biomolecular machine. While the overall structure of the injectisome is becoming increasingly well understood, the structural dynamics that regulate secretion remain unresolved. Particularly important for the functional regulation of type 3 secretion are the cytosolic injectisome proteins which transiently associate with injectisomes and whose structural dynamics and function remain incompletely understood. Here, we use long-exposure single-molecule localization microscopy to quantify the bound times of the cytosolic components SctQ, SctL, and SctN, at the injectisome of *Yersinia enterocolitica* in chemically induced secretion ON and OFF states and in the presence and absence of effector proteins. In the absence of effector proteins, each component exhibits distinct short-lived binding behavior on a timescale of seconds. The presence of the effector protein YopE increases bound times and synchronizes binding behavior across components, even without active secretion. Upon activation of secretion, a subpopulation of long-lived binding events emerges for SctQ, SctL, and SctN even within the same injectisomes, indicating that binding behavior between these proteins is secretion state-dependent and cooperative. These findings establish that the dynamic interactions between cytosolic injectisome proteins are modulated by the presence of secretion substrates and by secretion activating signals. Understanding the protein structural dynamics that underpin these modulations thus likely holds the key to understanding functional regulation of type 3 secretion.

INTRODUCTION

Type III secretion systems (T3SSs) are conserved multi-membrane spanning protein complexes used by many Gram-negative pathogens to assemble either flagella or injectisomes that translocate effector proteins directly into eukaryotic cells[1]. The injectisome includes a membrane-embedded export apparatus connected through the bacterial envelope to an extracellular needle (Fig. 1a). Substrates are engaged and prioritized for secretion through a cytosolic protein network[2-5].

In *Yersinia enterocolitica*, the expression and secretion of effector proteins are tightly regulated by the *yop* regulon, which responds to environmental cues such as temperature and calcium concentration. Induction of the *yop* regulon, along with the low-calcium response, provides tunable experimental parameters for toggling secretion activity and has been used extensively to model secretion-ON and -OFF states of the system[6-8]. Under high-calcium conditions, secretion is repressed and effectors accumulate within the bacterial cytosol, whereas calcium depletion activates the injectisome and triggers effector translocation across the host membrane. This reversible calcium switch enables controlled interrogation of the system's functional state. The post-secretion state, i.e. a secretion OFF state after secretion has occurred at least once, offers mechanistic value because it reveals how the cytosolic components are distinct from their involvement in initial injectisome assembly, thereby probing the involvement of cytosolic components in ON/OFF transitions.

59 Cryo-electron tomography and in situ structural studies have converged on an
60 architectural model in which the export apparatus is capped on its cytosolic face by a
61 multiprotein assembly comprising SctK, SctQ, and SctL, arranged around the hexameric
62 ATPase SctN and its central stalk[2,3,9,10]. Initial in situ observations using *Shigella* and
63 *Salmonella* minicell-producing mutants revealed six distinct cytoplasmic "pods" that
64 tether SctN to the membrane-embedded SctD ring[2,11,12]. In contrast, cryo-focused ion
65 beam milling followed by tomography in *Yersinia* revealed more continuous, ring-like
66 densities beneath the injectisome, reminiscent of the flagellar C ring[13,14]. These densities
67 are composed of SctK, SctQ, and likely $SctQ_C$, the alternatively expressed C-terminal
68 fragment of SctQ[15,16], while SctL retains a six-fold symmetric spoke-like arrangement
69 cradling SctN. Protein-protein interaction studies using bacterial hybrid systems[17-19] and
70 photo-crosslinking[20] have mapped a sequential SctK–Q–L–N arrangement, with SctQ
71 playing a particularly enigmatic role. Its N-terminal domain has been implicated in
72 interactions with SctK[20], $SctQ_C$[21], SctN[18], SctD[22], and even chaperone–effector
73 complexes[18,19,23]. Together, these studies define the physical stage on which dynamic
74 interactions occur, but they do not resolve how the cytosolic architecture reconfigures
75 under secretion-ON versus secretion-OFF conditions in live cells. Despite evidence for
76 complex formation in vitro, the functional relevance of these interactions, and how they
77 respond to environmental cues that toggle secretion remains unclear.

78 Complementing these structural insights, biochemical and genetic studies have
79 illuminated a functional role for the cytosolic injectisome proteins in substrate hierarchy. A
80 high molecular weight complex comprising SctK, SctQ, and SctL was shown to coordinate

81 the sequential loading of translocases and effector proteins, guided by dedicated
82 chaperones that ensure proper secretion order[24]. Using native gel electrophoresis and
83 subcellular fractionation in *Salmonella*, this study demonstrated that the so-called "sorting
84 platform" remains intact even in the absence of the needle complex, suggesting it
85 assembles independently and may serve as a pre-assembled substrate queue. Disruption
86 of this sorting platform impairs secretion efficiency and abolishes substrate prioritization,
87 underscoring the regulatory importance of this cytosolic interface. Whether similar
88 organizational principles apply across species remains to be determined. Thus, although
89 the static molecular framework of the injectisome and cytosolic injectisome complexes is
90 increasingly well-studied, the kinetics and regulation of protein exchange at the
91 injectisome remain largely unknown.

92 Fluorescence-recovery-after-photobleaching (FRAP) experiments in living cells have
93 shown that the cytosolic interface of the injectisome is highly dynamic. In *Yersinia*, SctQ
94 exchanges between injectisome-bound and cytosolic pools with a recovery half-time of
95 roughly one minute, accelerating under secreting conditions and requiring ATPase
96 activity[25]. These data indicate that SctQ binding and unbinding is connected to secretion
97 activity. Single-molecule tracking by our lab and others, in *Y. enterocolitica* subsequently
98 revealed that SctQ, SctL, and SctN populate multiple diffusive states in addition to an
99 injectisome-bound state, consistent with transient hetero-oligomeric subcomplexes that
100 assemble and disassemble on the timescale of seconds[26,27]. More recent work showed that
101 chaperones facilitate a cytosolic handover of effector proteins to SctQ-containing
102 complexes[28]. These SctQ- and effector-containing complexes are proposed to shuttle

103 substrates to the injectisome, implying that substrate availability informs both the
104 composition of cytosolic complexes and their binding/bound time to the injectisome[23,28,29].
105 Together, these observations suggest a dynamic picture in which cytosolic complex
106 formation, substrate loading, and injectisome engagement are kinetically coupled.

107 Here, we use long-exposure single-molecule localization to extract bound-time
108 distributions (also referred to as residence times) of SctQ, SctL, and SctN at the
109 injectisome of *Y. enterocolitica* in effector-free and YopE-expressing backgrounds under
110 secretion-OFF and ON conditions. In parallel, 3D single-molecule tracking characterizes
111 the bound fraction of SctQ as a proxy for k_{on} under different secretion states and the
112 presence of YopE. This approach allows us to test whether secretion state and effector
113 presence differentially regulate the binding kinetics and the associated number of
114 resolvable bound states. By quantifying these kinetics across defined environmental and
115 substrate conditions, we provide a quantitative framework describing how the T3SS
116 cytosolic proteins dynamically adjust the bound time in response to secretion demand and
117 effector availability.

118 **RESULTS**

119 To quantify the bound times of cytosolic T3SS components at the injectisome, we
120 used a biosafety leveadjusttible *Yersinia enterocolitica* strain lacking six major effector
121 proteins referred to as $T3SS^{\Delta effector}$ (also known as IML421asd)[4]. We expressed Halo-tagged
122 SctQ and SctL from their native loci via allelic exchange, while Halo-SctN was expressed
123 from a plasmid due to unsuccessful allelic replacement attempts. All fusion proteins were
124 confirmed to be stable (Fig. S1a) and functional (Fig S1b), i.e. capable of reversible
125 induction by the calcium effect (Fig S1c). These strains thus allowed us to probe the
126 binding behavior of SctQ, SctL, and SctN in the absence of effector interactions.

127 Halo-fused proteins were visualized with a low concentration of dye coupled with
128 long-exposure imaging, so that fast-moving molecules blur into the background, and
129 stationary, injectisome-bound proteins are detected as sharp point spread functions (Fig
130 1b). The pooled bound times were displayed as probability density function (pdf)-
131 normalized histograms and fit with single- or bi-exponential decays. The resulting bound
132 time fit (τ) of each protein at the injectisome follows an exponential decay and is the
133 inverse of the dissociation rate k_{off}.

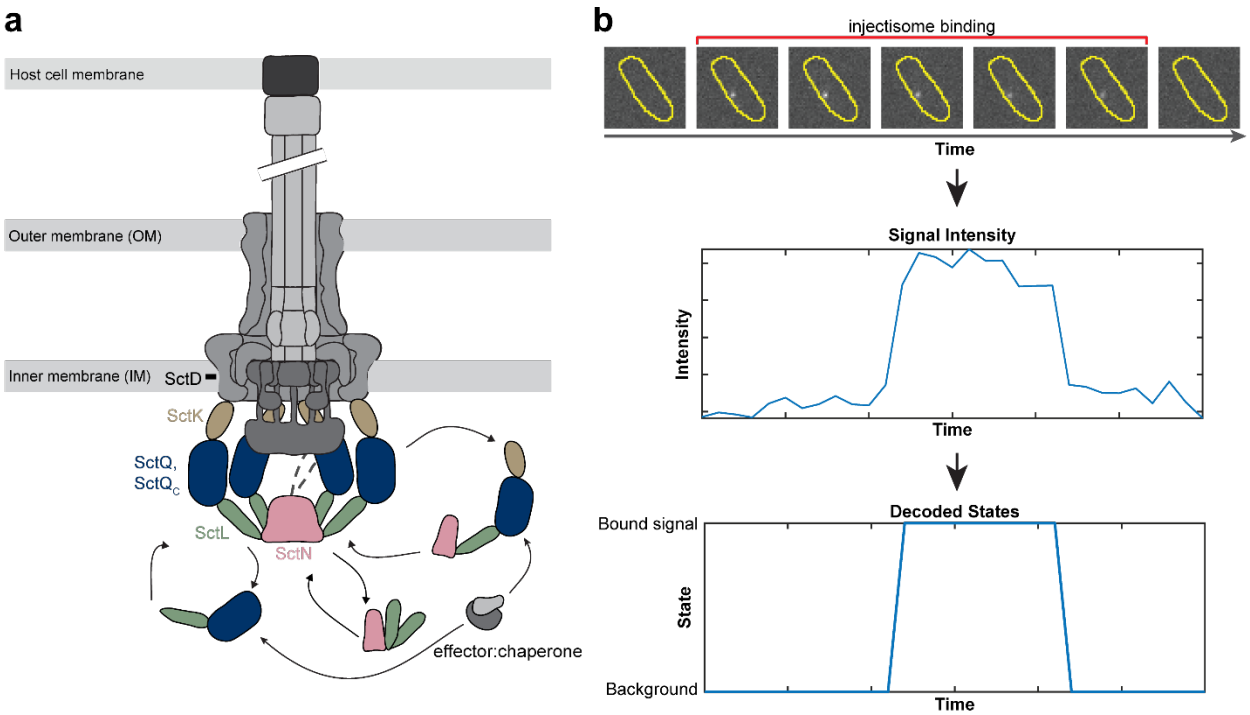

Figure 1: (a) Schematic of the Type III Secretion System (T3SS) architecture in *Yersinia enterocolitica*, highlighting the substructures and the cytosolic components analyzed in this study: SctQ, SctL, and SctN. **(b)** Schematic of the long-exposure imaging strategy used to extract bound times from stationary single-molecule trajectories. Fast-diffusing cytosolic molecules blur into the background, while stationary, injectisome-bound molecules appear as sharp point spread functions. This strategy enables direct measurement of bound times at the injectisome.

Effector-Free Conditions Reveal Distinct Binding Dynamics for Injectisome-Associated Proteins SctQ, SctL, and SctN

In the T3SS$^{\Delta effector/OFF}$ condition, the bound time histograms of SctQ, SctL and SctN are explained best by single exponential decays (Fig. 2a-c). Notably, all three proteins exhibit bound times on the order of a few seconds, but the fitted average bound times are all distinct. SctQ exhibits the shortest average bound time, τ = 2.5 s [2.4, 2.5], while the average bound times of SctL and SctN are slightly longer, τ = 3.4 s [3.3, 3.4] and τ = 3.0 s [2.9, 3.0], respectively (99% confidence intervals are indicated in square brackets).

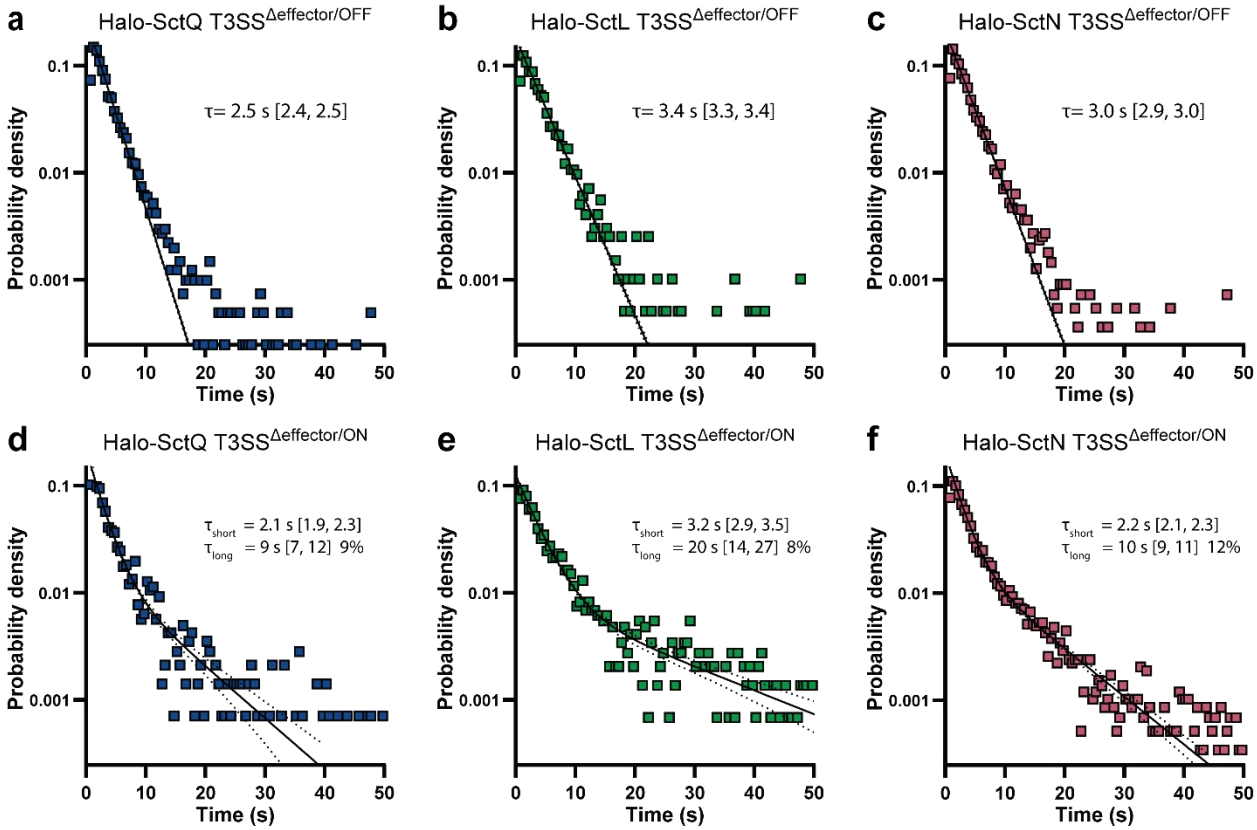

Figure 2: Distinct bound times for SctQ, SctL, and SctN and emergence of long-lived binding events under secretion ON conditions. Bound time distributions for Halo-tagged SctQ, SctL, and SctN under secretion OFF (top row) and ON (bottom row) conditions in the effector-free background. **(a–c)** Under secretion OFF conditions, all three proteins exhibit mono-exponential decay kinetics with distinct bound times: SctQ (τ = 2.5 s), SctL (τ = 3.4 s), and SctN (τ = 3.0 s). **(d–f)** Under secretion ON conditions, a subpopulation of long-lived binding events emerges for all proteins, requiring bi-exponential fits. Long-lived events comprise 9% (SctQ), 8% (SctL), and 12% (SctN) of trajectories, indicating two binding states at the injectisome. a) n = 4063 counts, b) n = 1973 counts, c) n = 5545 counts, d) n = 1417 counts, e) n = 1463 counts, f) n = 5857 counts.

Under secretion ON conditions, we observed a distinct shift in the binding behavior of SctQ, SctL, and SctN at the injectisome. Rather than a uniform change in average bound time, the data revealed a subpopulation of binding events with substantially longer durations (>10 s), prompting bi-exponential fits to the bound time distributions. These long-lived events comprised approximately 9% of SctQ, 8% of SctL, and 12% of SctN trajectories (Fig. 2d-f), suggesting the emergence of two binding modes at the injectisome. The finding

167 of long-lived states across all three proteins points to a coordinated and potentially
168 cooperative injectisome-bound configuration under secretion ON conditions.

169 Notably, the majority of binding events remained short-lived, and the fast
170 component of the bi-exponential fit was shorter under ON than OFF conditions: for
171 example, SctQ's short-term bound time decreased from 2.5 s (OFF) to 2.1 s (ON). When
172 considering both short- and long-lived events, the weighted average bound times were 2.7
173 s for SctQ, 4.4 s for SctL, and 3.1 s for SctN under $T3SS^{\Delta effector/ON}$ conditions.

174 As mentioned before, SctQ binding and unbinding have previously been measured
175 using fluorescence recovery after photobleaching (FRAP), an ensemble technique that
176 reports on the average recovery behavior of a population. Published FRAP measurements
177 showed a recovery half-time of 68.2 ± 7.9 s under secreting conditions, compared to 134.3
178 ± 16.1 s under non-secreting conditions[25], representing an overall faster recovery for
179 $T3SS^{\Delta effector/ON}$. Interestingly, despite the dominance of short-lived events in our single-
180 molecule data, the average bound times did not skew toward faster exchange as might be
181 expected from the FRAP results. This raised the question of whether individual
182 injectisomes engage in both short- and long-lived binding, or whether distinct classes of
183 injectisomes specialize in one mode over the other.

184

185 **The Same Injectisome Can Engage in Short- and Long-Term Binding**

186 Each single-molecule binding event can be precisely localized to a specific
187 subcellular location. Within the same bacterial cell, we observed both short- and long-lived

binding events for SctQ, SctL, and SctN (Fig. 3a), establishing that the emergence of long-lived states is not due to cell-to-cell variation. In this context, repeated binding at a given spatial location, i.e. a cluster, can be used as a proxy for the position of injectisomes (specifically its binding sites). To assess whether long-lived binding events preferentially occur at a distinct subset of injectisomes, we clustered binding events within each field of view using DBSCAN (ε = 150 nm, minPts = 2) and classified events as long if their bound time exceeded 30 frames (i.e. 15 seconds). Across all three proteins, we observed a range of behaviors; injectisomes with multiple binding events can be classified as showing exclusively short-lived events, exclusively long-lived events, and mixed binding profiles (Fig. 3b, table S2).

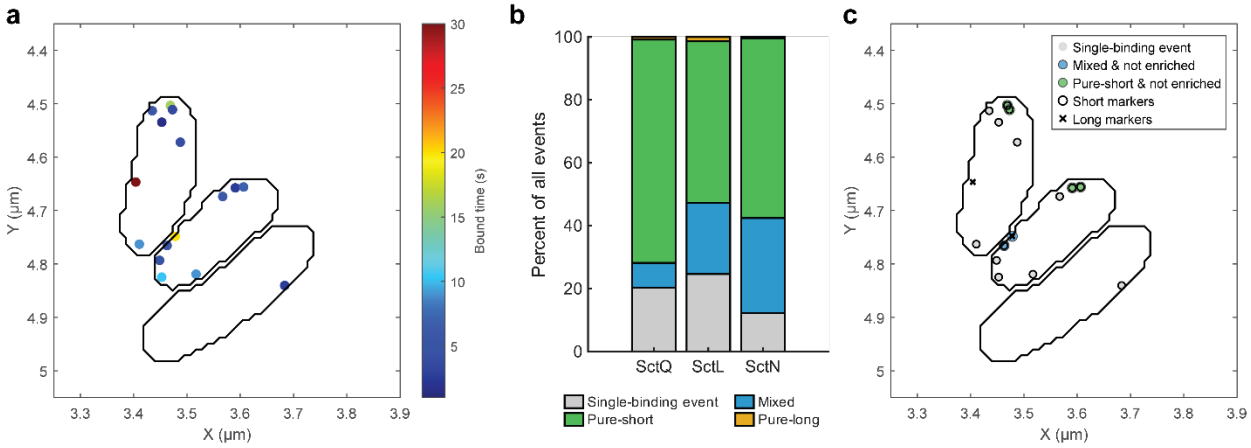

Figure 3: Short- and long-lived binding events occur at the same injectisome. (a) Representative cells showing spatial co-localization of short- and long-lived binding events for SctQ, SctL, and SctN, confirming that both binding modes occur within the same cell and at the same subcellular locations. **(b)** Classification of injectisomes based on binding profiles: mixed (both short and long), short-only, and long-only. **(c)** Statistical analysis using a hypergeometric test with FDR correction reveals no significant enrichment of long-lived events at specific clusters, suggesting that binding mode heterogeneity is not spatially segregated but reflects dynamic behavior at individual injectisomes. Parameters: ε = 100 nm, minPts = 2; long = dwell ≥ 30 frames.

207 It is important to note that these data were obtained by sparely labeling the proteins of
208 interest. The classification could therefore be skewed because we are not sampling all the
209 possible binding events at a given injectisome. We therefore compared the observed
210 fraction of long events within clusters to the global fraction of long events across the field
211 using a hypergeometric test with Benjamini–Hochberg correction ($\alpha = 0.05$). No clusters
212 showed significant enrichment of long events for any protein, indicating that long-lived
213 binding events were not spatially localized beyond random expectation. We repeated this
214 analysis for short binding events and again observed no statistical evidence for
215 enrichment. We therefore conclude that long- and short- lived bound states are not
216 spatially segregated and occur at the same injectisome.

217 **YopE Modulates Injectisome Binding Dynamics, With SctQ Showing Distinct**
218 **Sensitivity Across Secretion States**

219 To determine how the presence of effector proteins influences injectisome-
220 associated protein dynamics, we quantified the bound lifetimes of SctQ, SctL, and SctN
221 under secretion ON and OFF conditions in the presence of the effector protein YopE. YopE
222 was constitutively expressed from a plasmid and confirmed to be successfully secreted in
223 all strains (Fig S1b).

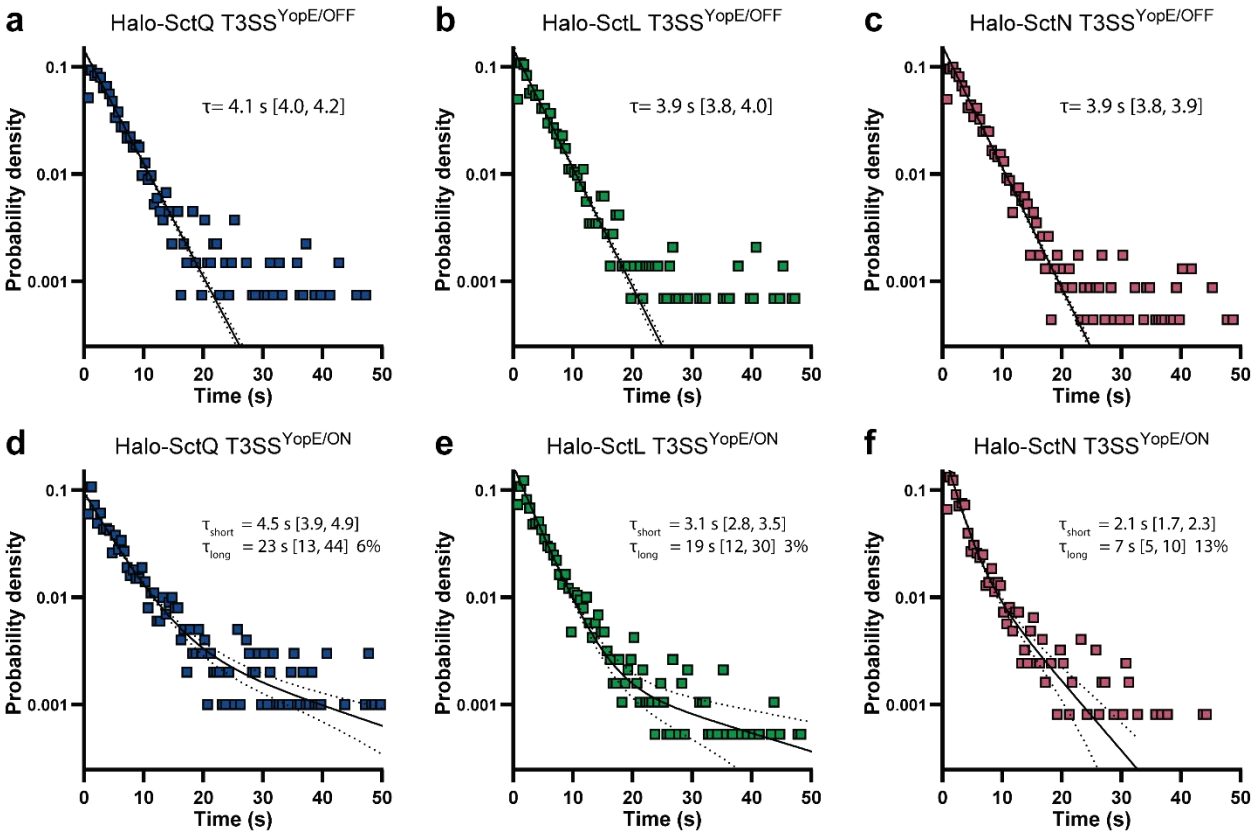

Figure 4: Effector presence increases bound times and synchronizes binding behavior. Bound time distributions for SctQ, SctL, and SctN under secretion OFF (top row) and ON (bottom row) conditions in the presence of the effector protein YopE. **(a–c)** Under secretion OFF conditions, all three proteins show increased bound times compared to the effector-free background, with mono-exponential fits yielding $\tau \approx 4$ s for all proteins. **(d–f)** Under secretion ON conditions, SctQ exhibits both an increased short-term bound time ($\tau = 4.5$ s) and a distinct long-lived subpopulation ($\tau = 23$ s, 6% of events). SctL and SctN show smaller changes, indicating component-specific sensitivity to effector presence. a) n = 1345 counts, b) n = 1446 counts, c) n = 2292 counts, d) n = 1003 counts, e) n = 1902 counts, f) n = 1240 counts.

All three proteins exhibited increased bound times compared to the effector-free condition ($T3SS^{\Delta effector/OFF}$), and their averaged bound times converged to statistically indistinguishable values (Fig. 4a-c). Specifically, mono-exponential fits yielded average bound times of τ = 4.1 s [4.0, 4.2] for SctQ, τ = 3.9 s [3.8, 4.0] for SctL, and τ = 3.9 s [3.8, 3.9] for SctN. The increase was most pronounced for SctQ, which nearly doubled its average bound time relative to the effector-free condition. These findings indicate that effector presence alone,

independent of active secretion, can increase the bound time of cytosolic components at the injectisome. We next asked whether these effects persist during active secretion ($T3SS^{YopE/ON}$).

Under secretion ON conditions, the presence of YopE modulates the binding dynamics of injectisome-associated proteins in a component-specific manner (Fig. 4d-f). Like in $T3SS^{\Delta effector/ON}$, this $T3SS^{YopE/ON}$ secretion condition revealed a subpopulation of binding events with substantially longer durations (>10 s), prompting bi-exponential fits to the bound time distributions. These long-lived events comprised approximately 6% of SctQ, 3% of SctL, and 13% of SctN trajectories (Fig. 4d-f), again suggesting the emergence of two binding modes at the injectisome. These two binding modes were evaluated using similar methods as before and we again observed mixed (long and short) binding behavior at the same injectisome (Table S3). In addition, there was no statistical evidence for enrichment of one type of binding at specific spatial locations (Fig S3), ruling out the possibility of two distinct classes of injectisomes. SctQ exhibits the longest short-term bound time (τ = 4.5 s [3.9, 4.9]), while the short-bound times of SctL and SctN are shorter, τ = 3.1 s [2.8, 3.5] and τ = 2.1 s [1.7, 2.3], respectively.

Secretion State Modulates Cytosolic Diffusion, Not Injectisome-Bound Fraction, of SctQ Independently of Effector Presence

The observation that SctQ exhibits slightly longer bound times on average under secreting conditions does not match previous FRAP measurements that indicate increased

261 protein exchange under secreting conditions which are proposed to facilitate effector
262 secretion. However, our bound time measurements do not rule out changes in the
263 association rate constant (k_{on}), thereby resulting in a distinct secretion on/off states. To
264 explore this possibility, we quantified the rate of appearance of fluorescence foci in the
265 bound-state data as a proxy for k_{on}. This provides an estimate of the on-rate per cell over
266 the imaging period, normalized to the total number of fluorescently active molecules in a
267 cell (Fig. S4). This quantification suggests that SctQ appearance rate decreases 4-fold in
268 the secretion ON state while the effect of YopE presence is minimal. However, because
269 this metric is normalized to total cellular fluorescence, some variation is expected, and
270 small shifts are difficult to interpret with high confidence. To verify the role of cytosolic
271 and/or injectisome remodeling of Halo-SctQ in light of effector protein changes *and*
272 secretion-state dependence, which may be connected to k_{on}, we employed 3D single-
273 molecule localization and tracking microscopy.

274 We have previously published eYFP-SctQ tracking results for *Y. enterocolitica* under
275 secretion-on conditions and found cytosolic states in addition to a prominent stationary
276 state corresponding to injectisome-bound SctQ proteins[26,27]. Similarly, for Halo-SctQ,
277 under all conditions, there exist both slow, membrane associated states, as well as
278 cytosolic diffusing states (Fig. 5a). We focused on the slowly diffusing population; the
279 fraction of slow-moving SctQ trajectories (mean displacement < 4 nm/ms) serves as a
280 proxy for injectisome association and is conceptually linked to the association rate
281 constant (k_{on}). An increase in k_{on} would increase the fraction of injectisome bound
282 molecules, especially if bound time remains constant or increases. Alternatively, under

283 saturating conditions, all binding sites may already be occupied regardless of secretion
284 state, in which case we expect bound fraction to remain constant across conditions as
285 well. We quantified this fraction to assess injectisome association (Fig. 5b). While this
286 metric showed statistically significant (Kruskal–Wallis, $p<0.05$) differences across
287 conditions, the observed variation was small prompting us to verify other indicators of
288 injectisome engagement.

289 To alternatively assess potential variations in injectisome association, we
290 implemented an approach based on spatial clustering of single-molecule localizations. By
291 identifying localization clusters (these were found at the membrane, i.e. consistent with
292 injectisome locations) (Fig S5a) and classifying trajectories as cluster-associated or not, we
293 obtained an alternative more direct measure of injectisome binding. This analysis also
294 revealed that the fraction of cluster-associated trajectories did not change drastically
295 across conditions (Fig. 5c), indicating that the injectisome-bound fraction of SctQ does not
296 vary substantially with secretion state or effector presence. We can thus interpret the
297 bound time changes (i.e. k_{off} variations), in the absence of strong evidence for counter k_{on}
298 changes.

299

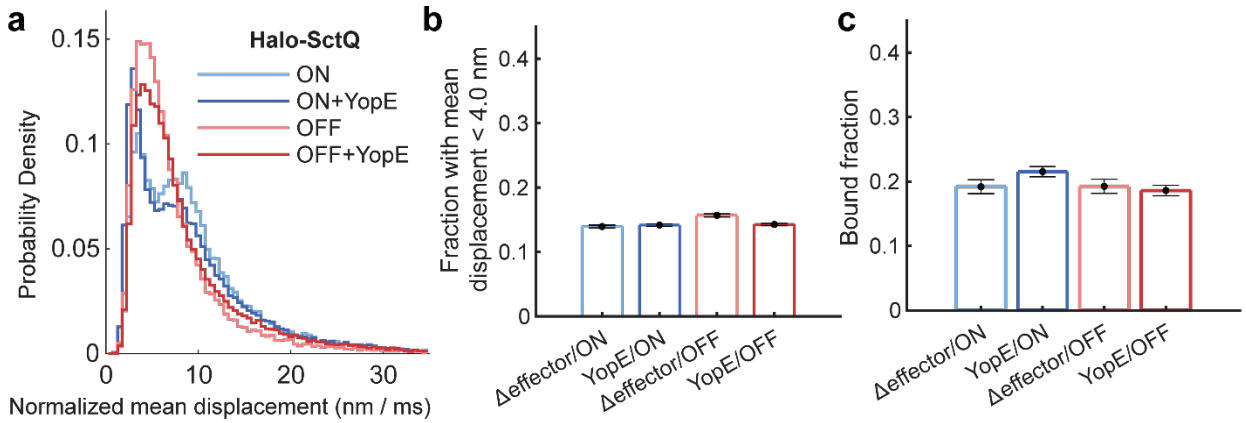

Figure 5: Secretion state modulates cytosolic diffusion of SctQ independently of effector presence. (a) Representative single-molecule trajectories of Halo-SctQ under four experimental conditions. **(b)** Quantification of the fraction of slow-moving trajectories (mean displacement < 4 nm/ms) per cell, used as a proxy for injectisome association. **(c)** Cluster-based analysis of single-molecule localizations confirms consistent injectisome-bound fractions across conditions, indicating that secretion state alters cytosolic diffusion but not the fraction of injectisome-engaged SctQ.

The shape differences in the distributions shown in Fig 5a further show different cytosolic diffusion behavior of SctQ in secretion ON and OFF conditions, potentially reflecting changes in cytosolic subcomplex formation. This occurs independently of the YopE-driven changes in k_{off} which we may conclude occur specifically at or when binding to the injectisome. Together, these results reveal that secretion state, but not effector presence, exert component-specific effects on cytosolic injectisome protein dynamics, both at the injectisome and in the cytosol.

DISCUSSION

During infection, *Yersinia enterocolitica* must rapidly adapt to changing host environments, including rapid transitions between secretion ON and OFF states thought to be essential for both immune evasion and efficient colonization[30-34]. Activation of secretion, as well as deactivation, occurs rapidly[34,35] and the ability of *Y. enterocolitica* to respond to these external stimuli suggests a strong external sensing mechanism that modulate how (cytosolic) components of the injectisome function.

Here, we measured the bound times of SctQ, SctL, and SctN under secretion OFF and ON conditions in the presence and absence of the effector protein YopE. In secretion OFF conditions, we observed mono-exponential decay kinetics for SctQ, SctL, and SctN, indicating a single, transient bound state at the injectisome for each cytosolic complex protein. In the absence of effectors ($T3SS^{\Delta effector}$), each protein exhibited a distinct fitted bound time, SctQ having the shortest, followed by SctN and SctL, suggesting that these components do not both bind *and* unbind as a coordinated unit.

In contrast, the fitted bound times of all three proteins converged to approximately 4 seconds in the presence of the effector protein YopE. This synchronization of bound times suggests that effector presence alone, independent of active secretion, can modulate the binding kinetics of cytosolic components. This observation also suggests that effectors may be preloaded onto injectisomes in the secretion OFF state priming the system for rapid activation. At the molecular level, the convergence of bound times may reflect a shift toward a more uniform or stabilized interaction mode, potentially due to effector-induced

336 conformational remodeling of cytosolic injectisome complexes prior to secretion.
337 Convergence of bound times also raises the likelihood that SctQ, SctL, and SctN bind and
338 unbind as a part of the same subcomplex. An alternative explanation to intact subcomplex
339 dissociation would be that all other proteins disassemble immediately after at least one of
340 them unbinds from the injectisome. Such a model is supported gene deletion studies that
341 have established that cytosolic injectisome proteins are mutually dependent on each other
342 injectisome binding[2,25,36,37], expression of each protein is required for injectisome
343 assembly[2,11,38] and type 3 secretion[17-19,39,40].

344 Under secretion ON conditions, SctQ, SctL, and SctN all displayed a subpopulation
345 of long-lived binding events, resulting in bi-exponential decay kinetics. Detection of this
346 long-lived binding state is uniquely enabled by single-molecule measurements, which
347 allow direct quantification of injectisome bound times of individual protein molecules.
348 Importantly, we observed both short- and long-lived binding events at the same subcellular
349 locations, suggesting that individual injectisomes can engage proteins in different binding
350 modes, one mode being more stable than the other. This raises the intriguing possibility of
351 functional asymmetry within a single injectisome, either through structural heterogeneity
352 across pods or through dynamic switching between distinct operational states in time (our
353 pooled single-molecule data were obtained over a timescale of ~20 minutes). In support of
354 the structural heterogeneity hypothesis, cryoEM studies have shown that the ATPase SctN
355 forms an asymmetric hexamer at the base of the injectisome[41], raising the possibility that
356 asymmetry extends to other cytosolic injectisome components and contributes to the
357 observed kinetic heterogeneity. Future structural and computational studies will be

358 essential to determine whether the short and long bound states correspond to distinct
359 conformational or functional states of the injectisome under defined secretion conditions.

360 Among the three cytosolic components analyzed, SctQ consistently exhibited the
361 most pronounced changes in bound time across conditions and was particularly sensitive
362 to the presence of the effector protein YopE. Under secretion OFF conditions, the addition
363 of YopE nearly doubled SctQ bound time, bringing it into close alignment with SctL and
364 SctN. Under secretion ON conditions, SctQ again showed heightened sensitivity, with both
365 an increased short-term bound time and a long-lived subpopulation. This component-
366 specific response supports the notion that SctQ may serve in a key regulatory role within
367 the assembled injectisome.

368 Single-molecule tracking revealed that the injectisome-bound fraction of SctQ does
369 not vary substantially with secretion state or YopE effector presence. When modest
370 changes in bound time occur, such as a shift in secretion state within the same strain
371 ($T3SS^{\Delta effector}$ or $T3SS^{YopE}$), we can interpret these while recognizing that there are no
372 indications for large swings in k_{on}. Interestingly, our single-molecule tracking data suggests
373 that SctQ does undergo secretion-dependent remodeling in the cytosol, while the
374 presence of YopE did not appear to influence this behavior. Indeed, we did not observe
375 direct evidence for distinct YopE-containing SctQ complexes in the cytosol under secreting
376 or post-secreting conditions. The absence of a YopE effect is intriguing, especially given
377 prior reports suggesting cytosolic effector–chaperone handover. One possibility to be
378 explored is that because SctQ participates in a range of cytosolic complexes[20,36,42], only
379 some of them may include YopE and these subcomplexes could be of similar size, making

380 it difficult to resolve effector-specific interactions. Alternatively, the changes in bound time
381 may not originate from altered cytosolic subcomplexes at all, but rather from effector-
382 induced alterations at the injectisome itself. For example, YopE may stabilize the cytosolic
383 injectisome complexes or modify the binding interface through allosteric effects that
384 prolongs SctQ binding. The fact that we observe strong changes in bound time without
385 corresponding shifts in cytosolic diffusion supports this possibility.

386 Comparing effector-free and YopE-expressing strains allowed us to separate the
387 effects of secretion state from those with effector involvement. The fact that cytosolic
388 injectisome protein binding kinetics are altered even in the absence of active secretion
389 supports the idea that cytosolic remodeling, potentially through effector or possible
390 effector–chaperone interactions, can precondition cytosolic injectisome proteins before
391 injectisome association. With a known ability to form multiple cytosolic
392 subcomplexes[15,17,27] the cytosolic injectisome proteins can act as a dynamic mediator that
393 integrates substrate availability with injectisome engagement.

394 In conclusion, the results reported here establish that cytosolic interactions and
395 local injectisome binding kinetics both correlate with secretion state and the presence of
396 YopE. The emergence of two distinct binding states under secretion ON conditions, at the
397 same injectisome, points to a dynamic secretion mechanism, with possible functional
398 asymmetry in space or time. The kinetic heterogeneity may arise either from structural
399 variation across injectisomes or through temporal switching between functional modes.
400 Understanding how these states arise and are regulated will be essential for refining
401 models of substrate selection and export in the T3SS.

402 **METHODS**

403 **Bacterial culture**

404 *Yersinia enterocolitica* strains were grown overnight in Brain Heart Infusion (BHI, Sigma-
405 Aldrich, St. Louis, MO) media supplemented with nalidixic acid (NaI) (35 µg/mL) and 2,6-
406 diaminopimelic acid (DAP) (80 µg/mL) at 28°C with shaking. Additional antibiotics were
407 included when appropriate: kanamycin (50 µg/mL) and/or chloramphenicol (25 µg/mL). On
408 the day of imaging, overnight culture was back diluted to a target OD_{600} of 0.1-0.3 and
409 grown at 28°C with shaking for 1-1.5 h. For secreting conditions, glycerol (4 mg/mL),
410 $MgCl_2$ (20 mM), and EGTA (5 mM) were then added to the culture, and the culture was
411 transferred to a 37°C water bath or incubator with shaking, for 3h to induce expression of
412 the *yop* regulon and ensure secretion activation. For non-secreting conditions (post-
413 secretion), cells were pelleted by centrifugation at 5,000 × *g* for 3 min and resuspended
414 with fresh BHI supplemented with NaI, DAP, $CaCl_2$ (5 mM) and grown for an additional hour.

415

416 **Strains and Plasmids**

417 Plasmids were constructed using Gibson Assembly. Briefly, DNA fragments with
418 overlapping ends were generated by Q5 PCR (New England Biolabs (NEB), Ipswich, MA) and
419 assembled in a single isothermal reaction. Assembled plasmids were transformed into
420 chemically competent *dh5α E coli* (NEB) and plated on LB agar supplemented with the
421 appropriate antibiotic for selection. Individual colonies were cultured overnight, and
422 plasmid DNA was isolated using a commercial miniprep kit (Qiagen, Hilden, Germany).

423 Plasmid sequences were verified by long-read sequencing (Plasmidsaurus, Eugene, OR).

424 Plasmids were transformed into the appropriate *Yersinia Enterocolitica* strain by

425 electroporation.

426 List of oligonucleotides

Name	Sequence	Used for plasmid
OC116	cacaggaaacacattcaacaatgGCAGAAATCGGTACTGGCTTTCCATTCGACCC	*pAH12::halo-sctN*
OC117	ccgacccacccaattgGCCGGAAATCTCGAGCGTCGACAGCCAG	*pAH12::halo-sctN*
OC118	cattgttgaatgtgtttcctgtgtgggcgcgcc	*pAH12::halo-sctN*
OC119	caattgggtgggtcgggcggct	*pAH12::halo-sctN*
OC163	GTA CCA CGC GGC AGT AAA ATA TCA TCA TTT ATT TCT ACA TCA CTG CCC CTG CCG GC	*pACAC::YopE*
OC164	AGC CTC CAC CTA GCC TTC ACA TCA ATG ACA GTA ATT GCT GCA TCT GTT GCC CC	*pACAC::YopE*

427

428 List of plasmids

Plasmid	Genotype	Reference
1	*pAH12::halo-sctN*	this study
2	*pAH12::halo*	this study
3	*pAH12::mEYFP*	this study
4	*pACAC::YopE*	this study

429

430 List of Strains

Strain	Genotype	Reference
IML421asd (ΔHOPEMTasd)	MRS40 *yopOΔ12-427 yopE21 yopHΔ11-352 yopM23 yopP23 yopT135 Δasd*	[4]
AD4461	IML421*asd halo-sctQ*	[36]
ADTM4525	IML421*asd halo-sctL*	[36]
AD4165	IML421*asd ΔsctN*	[25]

431

432 **Secretion Assay**

433 Cultures were grown as above, to desired secretion state. A small volume of culture was

434 taken to measure the OD_{600}. Main culture was pelleted (20,000 × *g*, 10 min, 4°C) and syringe

435 filtered with a 0.22 µm PVDF filter (Millipore, Burlington, MA). Supernatant was mixed with

436 trichloroacetic acid (TCA) to a final concentration of 10% w/v and incubated overnight at
437 4°C to precipitate proteins within the supernatant. Proteins were collected (20,000 × *g*,
438 20 min, 4°C) and washed with cold acetone (20,000 × *g*, 20 min, 4°C). The pellet was dried
439 at room temperature and resuspended in reducing SDS-PAGE loading buffer (SDS [3%,
440 wt/vol], glycerol [7.5%, wt/vol], 1.5% beta-mercaptoethanol, 0.0125% w/v Coomassie blue,
441 buffered with Tris [37.5 mM]; pH 7.0). Loading volume was normalized across samples ran
442 on the same gel, and proteins were separated by SDS-PAGE on 4–20% polyacrylamide gels
443 (Bio-rad, Hercules, CA). For visualization, the gels were stained with Coomassie Blue and
444 imaged with Bio-rad Gel Doc EZ imager.

445

446 **In-gel fluorescence Assay**

447 Cultures were grown as above, to desired secretion state. HaloTag fusions were incubated
448 with JFX-554 (Promega, Madison, WI) for the last 30 min of culturing. A small volume of
449 culture was taken to measure the OD_{600}. Culture was pelleted (5,000 x *g*, 5 min) and lysed in
450 a buffer of 20 mM Tris HCl, 50 mM NaCl, pH 7.4, supplemented with 0.2 mg/mL of lysozyme
451 and cOmplete™, Mini, EDTA-free Protease Inhibitor Cocktail (Roche, Basel, Switzerland).
452 Samples were resuspended in SDS-PAGE loading buffer and heated for 5 minutes at 98°C
453 before loading. Loading volume was normalized across samples ran on the same gel, and
454 proteins were separated by SDS-PAGE on 4–20% polyacrylamide gels (Bio-rad). For
455 visualization of in-gel JFX-554 fluorescence, a Biorad ChemiDoc MP system was used.

456

457 **Cell Plating for Microscopy**

458 Cultures were grown as described above. In the case of HaloTag visualization, Janelia Fluor
459 HaloTag ligand dye, JFX-554 (Promega) was added to the culture 30 minutes prior to
460 imaging. The appropriate dye concentration was strain dependent: 0.5 nM for Halo-SctQ, 2
461 nM for Halo-SctL, 2nM for Halo-SctN. Cells were pelleted by centrifugation at 5,000 × *g* for
462 3 min and washed three times in fresh M9 minimal media. After the three washes, the
463 remaining pellet was resuspended in M9 supplemented with DAP, $MgCl_2$, glycerol, and
464 EGTA (secreting conditions) or $CaCl_2$. For super-resolution fluorescent imaging, fluorescent
465 fiducial markers (Invitrogen) were added to cell suspensions. Cells were finally plated on
466 1.5% agarose pads in M9 containing DAP and EGTA or $CaCl_2$.

467

468 **Optical Setup**

469 Image data were acquired on a custom-built inverted fluorescence microscope based on
470 the RM21 platform (Mad City Labs, Madison, WI), as previously described[26,43] . Immersion
471 oil was placed between the lens objective (UPLSAPO 100; numerical aperture [NA], 1.4)
472 and the glass coverslip (VWR, Radnor, PA; number 1.5; 22 mm by 22 mm). A 561 nm laser
473 (Coherent, Santa Clara, CA; Genesis MX561-4000 MTM) was used for excitation of JFX-554
474 (Promega Madison, WI) (~600 mW cm^{-2}). Zero-order quarter-wave plates (Thorlabs,
475 Newton, NJ, WPQ05M-561) were used to circularly polarize the excitation laser. A dichroic
476 mirror (Chroma zt440/488/561rpc) was used to separate excitation/activation light from
477 fluorescence emission of JFX-554. Fluorescence emission was passed through a filter set

478 including long-pass (514nm), short- pass (800 nm), and notch filter 561 nm/10bp
479 (Semrock, Rochester, NY; LP02-514RU-25, Chroma, Bellows Falls, VT; ET700SP-2P8, and
480 Chroma, Bellows Falls, VT; ZET561NF, respectively). In the case of 3D super-resolution
481 imaging, the emission path contains a wavelength-specific dielectric phase mask (Double
482 Helix, LLC, Boulder, CO) that is placed in the Fourier plane of the microscope to generate a
483 double-helix point spread function (DHPSF)[44,45]. The fluorescence signal is detected on a
484 scientific complementary metal oxide semiconductor (sCMOS) camera (Hamamatsu,
485 Bridgewater, NJ; ORCA-Flash 4.0 V2). A flip mirror in the emission pathway enables toggling
486 the microscope between fluorescence imaging and phase-contrast imaging modes without
487 having to change the lens objective of the microscope. Illumination for phase contrast
488 imaging was achieved with an LED at 625 nm (Thorlabs, Newton NJ; M625L3).

489 Imaging was performed on a custom-built, dual-color inverted fluorescence microscope.
490 The laser intensity was attenuated significantly. Up to 2500 frames were collected per field-
491 of-view with an exposure time of 500 ms.

492

493 **Long Exposure Data processing**

494 Broadly, image processing occurred in a two-step process. First, potential binding events
495 were identified using ThunderSTORM[46] generating regions of interest for further analysis.
496 Second, intensity traces over time were fitted with a Hidden Markov Model to distinguish
497 between a bound and background state.

Specifically, prior to PSF fitting, images from each field-of-view were background subtracted and cropped as needed. PSFs were fit using ThunderSTORM in ImageJ using the difference of Gaussians (DoG) filter option with a threshold of 1.5*std(Wave.F1)[46]. Candidate binding events were further narrowed down with a requirement for there to be a localization within 50 nm at least 2 times per 1000 frames. The image stack and its corresponding ThunderSTORM data was imported into MATLAB. Images were background subtracted, normalized and converted to photoelectron units. A simple nearest-neighbor linker associated detections across frames (distance threshold 300 nm; maximum frame gap 15) to form candidate bound trajectories.

For every frame within a trajectory, signal was quantified as the sum in a 5×5 pixel ROI centered on the trajectory position. Pooled photon values were modeled with a Gaussian mixture model (GMM; 3 components) to estimate background and signal intensity distributions. Per-track ROI time series were then segmented with a two-state hidden Markov model (HMM; background ↔ signal): initial state means/variances were set from the GMM, a conservative transition matrix was used and the most probable state sequence was decoded by Viterbi. Quality gates rejected traces with (i) peak intensity ≤ background upper bound, (ii) minimum intensity ≥ signal lower bound, (iii) dynamic range below the GMM-implied separation, or (iv) substantial signal/background standard-deviation overlap. Error codes were logged for each exclusion. In addition, any bound state event longer than 40 frames (20 seconds) was inspected and manually approved. Remaining signal segments were taken as valid dwell events; durations (frames) were converted to time using 0.5 s/frame and compiled across tracks.

Determination of t_{bound}

To characterize the distribution of bound-state lifetimes, dwell time measurements were extracted for each condition and protein variant and binned into normalized histograms. To reduce the influence of short-duration events on the fit, the first histogram bin (0-0.5 seconds), a group that is disproportionally undercounted, was excluded from model fitting. For each distribution, both single- and double-exponential decay models were fitted to the data using nonlinear least-squares regression. The single-exponential model was defined as $\mathrm{y(t)} = \mathrm{A\,e^{-\lambda\,t}}$ and the double-exponential model as $y(t) = A_1 e^{-\lambda_1 t} + A_2 e^{-\lambda_2 t}$ with time constants $\tau_i = \frac{1}{\lambda_i}$.

Model selection was based on comparison of the Akaike Information Criterion (AIC), with the bi-exponential model favored if AIC was reduced by more than 2 units. In addition, if a state in the bi-exponential fit contributed less than 2% of the population, the mono-exponential model was favored. Goodness-of-fit was assessed via the coefficient of determination (R^2). For each fit, 99% confidence intervals were estimated by propagation of uncertainty using the Jacobian and parameter covariance matrix. Fits and their confidence intervals were overlaid on probability density plots to visualize lifetime distributions for each experimental condition.

Cluster detection and enrichment analysis

540 Single-molecule trajectories of SctQ, SctL, and SctN recorded under secretion-ON
541 conditions were analyzed to test whether long-lived binding events were spatially enriched.
542 Approved trajectories were converted into individual binding events, each represented by
543 the mean localization position and event duration. Events lasting ≥ 30 frames were
544 classified as long.

545 Spatial event clusters were identified using DBSCAN (ε = 100 nm, minPts = 2). For each
546 field of view, the observed fraction of long events within each cluster was compared with
547 the global fraction of long events using a one-sided hypergeometric test. Resulting p-
548 values were corrected for multiple testing by the Benjamini–Hochberg procedure (α =
549 0.05), and significant clusters were optionally validated by 2,000 random label-shuffle
550 permutations. Clusters were categorized as mixed, pure-long, or pure-short based on the
551 composition of event durations.

552

553 **Super-resolution fluorescence imaging & Data Processing**

554 Up to 20,000 frames are collected per field of view with an exposure time of 25 ms. Phase
555 contrast images were taken before and after fluorescence imaging. Raw data were
556 processed in MATLAB using a modified version of easy-DHPSF software[26,47]. Fluorescent
557 fiducial markers were used for sample drift correction. Phase contrast images were
558 segmented using Omnipose[48]. Single-molecule localizations were registered to phase
559 contrast masks using a two-step affine transformation in MATLAB, as described

560 previously[26]. Localizations outside of cells were discarded from further analysis using axial
561 bounds and Omnipose-derived cell outlines.

562

563 **MSD / cumulative displacement tracking**

564 To derive single-molecule displacements, localizations in subsequent frames were linked
565 into trajectories. A maximum linking distance of 2.5 μm was used for linking analysis, and
566 multiple localizations that were present at the same time within a single cell were
567 discarded to prevent misassignment of molecules.

568 For each trajectory, the cumulative displacement was calculated as the running sum of all
569 stepwise displacements between consecutive localizations,

576 $$CD_n = \sum_{i=2}^{n} \sqrt{(x_i - x_{i-1})^2 + (y_i - y_{i-1})^2 + (z_i - z_{i-1})^2}$$

570 where x_i, y_i, z_i are the 3D coordinates of the molecule at frame i. The cumulative
571 displacement versus time relationship was used to visualize overall molecular motion and
572 to compute the mean step size or slope of displacement accumulation over time. This
573 slope provided a direct, model-free metric of apparent mobility for each trajectory. The
574 plotted mean displacement normalized by time is thus an average of this displacement,
575 which is equivalent to the slope of the cumulative displacement curve over time.

577 **REFERENCES**

578

579 1 Galán, J. E. & Collmer, A. Type III Secretion Machines: Bacterial Devices for Protein

580 Delivery into Host Cells. *Science* **284**, 1322-1328 (1999).

581 https://doi.org/doi:10.1126/science.284.5418.1322

582 2 Hu, B., Lara-Tejero, M., Kong, Q., Galán, J. E. & Liu, J. In Situ Molecular Architecture

583 of the Salmonella Type III Secretion Machine. *Cell* **168**, 1065-1074.e1010 (2017).

584 https://doi.org/http://dx.doi.org/10.1016/j.cell.2017.02.022

585 3 Butan, C., Lara-Tejero, M., Li, W., Liu, J. & Galán, J. E. High-resolution view of the type

586 III secretion export apparatus in situ reveals membrane remodeling and a secretion

587 pathway. *Proc Natl Acad Sci U S A* **116**, 24786-24795 (2019).

588 https://doi.org/10.1073/pnas.1916331116

589 4 Kudryashev, M. *et al*. In situ structural analysis of the Yersinia enterocolitica

590 injectisome. *Elife* **2**, e00792 (2013). https://doi.org/10.7554/eLife.00792

591 5 Miletic, S. *et al*. Substrate-engaged type III secretion system structures reveal gating

592 mechanism for unfolded protein translocation. *Nat Commun* **12**, 1546 (2021).

593 https://doi.org/10.1038/s41467-021-21143-1

594 6 Cornelis, G. R. The Yersinia Ysc-Yop 'type III' weaponry. *Nat Rev Mol Cell Biol* **3**, 742-

595 752 (2002). https://doi.org/10.1038/nrm932

596 7 Dewoody, R. S., Merritt, P. M. & Marketon, M. M. Regulation of the Yersinia type III

597 secretion system: traffic control. *Front Cell Infect Microbiol* **3**, 4 (2013).

598 https://doi.org/10.3389/fcimb.2013.00004

599 8 Mehigh, R. J., Sample, A. K. & Brubaker, R. R. Expression of the low calcium
600 response in Yersinia pestis. *Microb Pathog* **6**, 203-217 (1989).
601 https://doi.org/10.1016/0882-4010(89)90070-3
602 9 Diepold, A. & Wagner, S. Assembly of the bacterial type III secretion machinery.
603 *FEMS Microbiol Rev* **38**, 802-822 (2014). https://doi.org/10.1111/1574-6976.12061
604 10 Bergeron, J. R. C. & Marlovits, T. C. Cryo-EM of the injectisome and type III secretion
605 systems. *Curr Opin Struct Biol* **75**, 102403 (2022).
606 https://doi.org/10.1016/j.sbi.2022.102403
607 11 Hu, B. *et al*. Visualization of the type III secretion sorting platform of Shigella
608 flexneri. *Proc Natl Acad Sci U S A* **112**, 1047-1052 (2015).
609 https://doi.org/10.1073/pnas.1411610112
610 12 Makino, F. *et al*. The Architecture of the Cytoplasmic Region of Type III Secretion
611 Systems. *Scientific Reports* **6**, 33341 (2016). https://doi.org/10.1038/srep33341
612 http://www.nature.com/articles/srep33341#supplementary-information
613 13 Berger, C. *et al*. Structure of the Yersinia injectisome in intracellular host cell
614 phagosomes revealed by cryo FIB electron tomography. *Journal of Structural Biology*
615 **213**, 107701 (2021). https://doi.org/https://doi.org/10.1016/j.jsb.2021.107701
616 14 Diepold, A. & Armitage, J. P. Type III secretion systems: the bacterial flagellum and
617 the injectisome. *Philos Trans R Soc Lond B Biol Sci* **370** (2015).
618 https://doi.org/10.1098/rstb.2015.0020

619 15 Bzymek, K. P., Hamaoka, B. Y. & Ghosh, P. Two translation products of Yersinia yscQ
620 assemble to form a complex essential to type III secretion. *Biochemistry* **51**, 1669-
621 1677 (2012). https://doi.org/10.1021/bi201792p
622 16 Yu, X. J., Liu, M., Matthews, S. & Holden, D. W. Tandem translation generates a
623 chaperone for the Salmonella type III secretion system protein SsaQ. *J Biol Chem*
624 **286**, 36098-36107 (2011). https://doi.org/10.1074/jbc.M111.278663
625 17 Jackson, M. W. & Plano, G. V. Interactions between type III secretion apparatus
626 components from *Yersinia pestis* detected using the yeast two-hybrid system. *FEMS*
627 *Microbiology Letters* **186**, 85-90 (2000). https://doi.org/10.1111/j.1574-
628 6968.2000.tb09086.x
629 18 Morita-Ishihara, T. *et al.* Shigella Spa33 is an essential C-ring component of type III
630 secretion machinery. *J Biol Chem* **281**, 599-607 (2006).
631 https://doi.org/10.1074/jbc.M509644200
632 19 Spaeth, K. E., Chen, Y. S. & Valdivia, R. H. The Chlamydia type III secretion system C-
633 ring engages a chaperone-effector protein complex. *PLoS Pathog* **5**, e1000579
634 (2009). https://doi.org/10.1371/journal.ppat.1000579
635 20 Soto, J. E., Galan, J. E. & Lara-Tejero, M. Assembly and architecture of the type III
636 secretion sorting platform. *Proc Natl Acad Sci U S A* **119**, e2218010119 (2022).
637 https://doi.org/10.1073/pnas.2218010119
638 21 Bernal, I. *et al.* Molecular Organization of Soluble Type III Secretion System Sorting
639 Platform Complexes. *J Mol Biol* (2019). https://doi.org/10.1016/j.jmb.2019.07.004

640 22 Barison, N., Lambers, J., Hurwitz, R. & Kolbe, M. Interaction of MxiG with the
641 cytosolic complex of the type III secretion system controls Shigella virulence. *FASEB*
642 *J* **26**, 1717-1726 (2012). https://doi.org/10.1096/fj.11-197160
643 23 Wimmi, S. *et al*. Cytosolic sorting platform complexes shuttle type III secretion
644 system effectors to the injectisome in Yersinia enterocolitica. *Nat Microbiol* **9**, 185-
645 199 (2024). https://doi.org/10.1038/s41564-023-01545-1
646 24 Lara-Tejero, M., Kato, J., Wagner, S., Liu, X. & Galan, J. E. A Sorting Platform
647 Determines the Order of Protein Secretion in Bacterial Type III Systems. *Science*
648 **331**, 1188-1191 (2011). https://doi.org/10.1126/science.1201476
649 25 Diepold, A., Kudryashev, M., Delalez, N. J., Berry, R. M. & Armitage, J. P.
650 Composition, formation, and regulation of the cytosolic c-ring, a dynamic
651 component of the type III secretion injectisome. *PLoS Biol* **13**, e1002039 (2015).
652 https://doi.org/10.1371/journal.pbio.1002039
653 26 Rocha, J. M. *et al*. Single-molecule tracking in live Yersinia enterocolitica reveals
654 distinct cytosolic complexes of injectisome subunits. *Integr Biol (Camb)* **10**, 502-
655 515 (2018). https://doi.org/10.1039/c8ib00075a
656 27 Prindle, J. R., Wang, Y., Rocha, J. M., Diepold, A. & Gahlmann, A. Distinct Cytosolic
657 Complexes Containing the Type III Secretion System ATPase Resolved by Three-
658 Dimensional Single-Molecule Tracking in Live Yersinia enterocolitica. *Microbiol*
659 *Spectr* **10**, e0174422 (2022). https://doi.org/10.1128/spectrum.01744-22

660 28 Pintor, K. *et al*. In situ analysis of type III secretion chaperone proteins indicates a
661 cytosolic handover of virulence effectors. *FEMS Microbes* **6**, xtaf010 (2025).
662 https://doi.org/10.1093/femsmc/xtaf010
663 29 Gilzer, D., Schreiner, M. & Niemann, H. H. Direct interaction of a chaperone-bound
664 type III secretion substrate with the export gate. *Nat Commun* **13**, 2858 (2022).
665 https://doi.org/10.1038/s41467-022-30487-1
666 30 Grosdent, N., Maridonneau-Parini, I., Sory, M. P. & Cornelis, G. R. Role of Yops and
667 adhesins in resistance of Yersinia enterocolitica to phagocytosis. *Infect Immun* **70**,
668 4165-4176 (2002). https://doi.org/10.1128/iai.70.8.4165-4176.2002
669 31 Navarro, L., Alto, N. M. & Dixon, J. E. Functions of the Yersinia effector proteins in
670 inhibiting host immune responses. *Curr Opin Microbiol* **8**, 21-27 (2005).
671 https://doi.org/10.1016/j.mib.2004.12.014
672 32 Galán, J. E. Common themes in the design and function of bacterial effectors. *Cell*
673 *Host Microbe* **5**, 571-579 (2009). https://doi.org/10.1016/j.chom.2009.04.008
674 33 Zwack, E. E. *et al*. Inflammasome activation in response to the Yersinia type III
675 secretion system requires hyperinjection of translocon proteins YopB and YopD.
676 *mBio* **6**, e02095-02014 (2015). https://doi.org/10.1128/mBio.02095-14
677 34 Milne-Davies, B. *et al*. Life After Secretion-Yersinia enterocolitica Rapidly Toggles
678 Effector Secretion and Can Resume Cell Division in Response to Changing External
679 Conditions. *Front Microbiol* **10**, 2128 (2019).
680 https://doi.org/10.3389/fmicb.2019.02128

681 35 Enninga, J., Mounier, J., Sansonetti, P. & Tran Van Nhieu, G. Secretion of type III
682 effectors into host cells in real time. *Nat Methods* **2**, 959-965 (2005).
683 https://doi.org/10.1038/nmeth804
684 36 Diepold, A. *et al.* A dynamic and adaptive network of cytosolic interactions governs
685 protein export by the T3SS injectisome. *Nat Commun* **8**, 15940 (2017).
686 https://doi.org/10.1038/ncomms15940
687 37 Diepold, A. *et al.* Deciphering the assembly of the Yersinia type III secretion
688 injectisome. *EMBO J* **29**, 1928-1940 (2010). https://doi.org/10.1038/emboj.2010.84
689 38 Jouihri, N. *et al.* MxiK and MxiN interact with the Spa47 ATPase and are required for
690 transit of the needle components MxiH and MxiI, but not of Ipa proteins, through the
691 type III secretion apparatus of Shigella flexneri. *Molecular Microbiology* **49**, 755-767
692 (2004). https://doi.org/10.1046/j.1365-2958.2003.03590.x
693 39 Johnson, S. & Blocker, A. Characterization of soluble complexes of the Shigella
694 flexneri type III secretion system ATPase. *FEMS Microbiol Lett* **286**, 274-278 (2008).
695 https://doi.org/10.1111/j.1574-6968.2008.01284.x
696 40 Hueck, C. J. Type III Protein Secretion Systems in Bacterial Pathogens of Animals
697 and Plants. *Microbiology and Molecular Biology Reviews* **62**, 379-433 (1998).
698 41 Majewski, D. D. *et al.* Cryo-EM structure of the homohexameric T3SS ATPase-central
699 stalk complex reveals rotary ATPase-like asymmetry. *Nature Communications* **10**,
700 626 (2019). https://doi.org/10.1038/s41467-019-08477-7

42 Marcos-Vilchis, A. *et al*. On the role of the sorting platform in hierarchical type III secretion regulation in enteropathogenic Escherichia coli. *Journal of Bacteriology* **207** (2025). https://doi.org/10.1128/jb.00446-24

43 Rocha, J., Corbitt, J., Yan, T., Richardson, C. & Gahlmann, A. Resolving Cytosolic Diffusive States in Bacteria by Single-Molecule Tracking. *Biophys J* **116**, 1970-1983 (2019). https://doi.org/10.1016/j.bpj.2019.03.039

44 Pavani, S. R. P. *et al*. Three-dimensional, single-molecule fluorescence imaging beyond the diffraction limit by using a double-helix point spread function. *Proceedings of the National Academy of Sciences of the United States of America* **106**, 2995-2999 (2009). https://doi.org/10.1073/pnas.0900245106

45 Thompson, M. A., Lew, M. D., Badieirostami, M. & Moerner, W. E. Localizing and tracking single nanoscale emitters in three dimensions with high spatiotemporal resolution using a double-helix point spread function. *Nano Letters* **10**, 211-218 (2010). https://doi.org/10.1021/nl903295p

46 Ovesny, M., Krizek, P., Borkovec, J., Svindrych, Z. & Hagen, G. M. ThunderSTORM: a comprehensive ImageJ plug-in for PALM and STORM data analysis and super-resolution imaging. *Bioinformatics* **30**, 2389-2390 (2014). https://doi.org/10.1093/bioinformatics/btu202

47 Lew, M. D., von Diezmann, A. R. S. & Moerner, W. E. Easy-DHPSF open-source software for three-dimensional localization of single molecules with precision beyond the optical diffraction limit. *Protocol Exchange*, doi:10.1038/protex.2013.1026 (2013). https://doi.org/doi:10.1038/protex.2013.026

723 48 Cutler, K. J. *et al*. Omnipose: a high-precision morphology-independent solution for
724 bacterial cell segmentation. *Nat Methods* **19**, 1438-1448 (2022).
725 https://doi.org/10.1038/s41592-022-01639-4

726